Title

Multi-Technique Residual Stress Measurements to Quantify Stress Relief of 7085-T7452 Aluminum Die Forgings

Journal

Materials Performance and Characterization, 7(4)

ISSN

2379-1365

Authors

Olson, Mitchell D
Spradlin, Thomas J
DeWald, Adrian T
et al.

Publication Date

2018-11-07

DOI

10.1520/mpc20170105

Multi-Technique Residual Stress Measurements to Quantify Stress Relief of 7085-T7452 Aluminum Die Forgings

Mitchell D. Olson[1*], Thomas J. Spradlin[2], Adrian T. DeWald[1], and Michael R. Hill[3]
[1]*Hill Engineering, LLC, 3083 Gold Canal Drive, Rancho Cordova, CA, USA*
[2]*Air Force Research Laboratory, 1864 4th Street, Wright-Patterson AFB, OH, USA*
[3]*Department of Mechanical and Aerospace Engineering, University of California, Davis, One Shields Avenue, Davis, CA, USA*

Submitted for the Special Issue on Residual Stress in the
ASTM International Journal on Materials Performance and Characterization, July 2017
Submitted in Revised form, October 2017

Published as :Olson, M., Spradlin, T., DeWald, A., and Hill, M., "Multi-Technique Residual Stress Measurements to Quantify Stress Relief of 7085-T7452 Aluminum Die Forgings," Materials Performance and Characterization, v7(4), 2018. https://doi.org/10.1520/MPC20170105

ABSTRACT

This paper describes use of complementary residual stress measurements to quantify cold-work stress relief in die forgings used for monolithic unitized aerospace components. Two specimens were used, being nominally identical, but measured at different processing stages: one die forged and quenched (high residual stress state) and one having a post-quench, cold-work stress relief (low residual stress state). Multi-component residual stress maps were developed using multiple techniques along a single measurement plane (axes of this plane run parallel to the nominal long-transverse (*x*-direction) and short-transverse directions (*y*-direction)). The measurement techniques were energy dispersive X-ray diffraction (EDXRD), neutron diffraction (ND), and primary slice removal (PSR) biaxial mapping. Good agreement was found between the EDXRD and PSR biaxial mapping measurements. In the high-stress specimen, measured stress normal to the measurement plane (*z*-direction (L)) is highly compressive along the part exterior (-300 MPa) and highly tensile toward the center (+250 MPa), as typical of quenched aluminum. Stress along the *x*-direction has a similar spatial distribution but smaller magnitude (-200 MPa to +130 MPa). The measured stresses in the cold-worked, low-stress specimen are significantly lower, with *z*-direction and *x*-direction stresses ranging between -130 MPa and +75 MPa.

Keywords: Residual stress, aluminum die forging, 7085, energy dispersive X-ray diffraction, neutron diffraction, PSR biaxial mapping, contour method, slitting method, residual stress measurement

1. INTRODUCTION

The aerospace industry uses monolithic unitized components as primary aircraft structure, in place of multi-component assemblies to improve structural performance and reduce weight [1]. Structural performance improvements, within the context of these unitized components, comprise increased load

* Corresponding author. *E-mail address:* molson@hill-engineering.com

transfer efficiency through load path continuity. Due to manufacturing limitations and constraints, large unitized structural aluminum components are often machined from stress-relieved die forgings, which tend to have higher residual stress levels than other material forms (e.g., stress-relieved plate). The residual stress state of any component can affect its fatigue performance, making quantification of the residual stress state critical for accurate fatigue analysis. Therefore, both material providers and aircraft manufacturers have collaborated to address the issue using analytical tools and state-of-the-art residual stress measurement techniques at fatigue sensitive locations [2].

Recent advances in integrated computational materials engineering (ICME) provides an analytical prediction capability that considers both material property evolution and continuum based residual stress state development [3,4,5]. This technology has enabled the structural engineering community to incorporate the complete residual stress tensor at all spatial locations of a forged component into simulation based design and lifing analyses, forming the core of an integrated computational structural engineering (ICSE) concept [6]. Like any modeling effort, however, these models require empirical validation at key locations for every geometry and processioning combination. Amongst the plethora of residual stress measurement techniques available, there are two major families that are viable for poly-crystalline materials of typical die forging sizes: strain relief and particle diffraction.

For this application, the die forgings have a thickness of approximately 25 to 50 mm (1 to 2 in) at the selected measurement location. For the thicknesses of the measurement plane cross-section and desired spatial resolution are close to, or beyond, the capabilities of diffraction based techniques if all three strain components must be measured. Neutron diffraction is capable of measuring at the requisite thicknesses, but the gage volumes available are an order of magnitude larger than typically necessary. X-ray diffraction techniques, as currently implemented, can capture data at the correct spatial resolution but are unable to penetrate some of the required thicknesses.

The objective of this work is to determine the applicability of residual stress mapping using EDXRD, neutron diffraction, and PSR biaxial mapping in a thick and relatively flat area of forged aluminum and to compare the amount of stress relief due to cold working.

2. METHODS

2.1. Die-Forged 7085 Specimens

Two 7085 aluminum die forgings were used for these residual stress measurements. Both specimens started as 7085 aluminum die forgings that were heat treated to a -T74 temper. One was subsequently cold compressed to a -T7452 temper using dedicated cold-working dies [7]. The heat treatment consisted of solution treatment at 480 °C (895 °F) in an air furnace for 2 hours, followed by immersion quenching in water. Before and after cold compression, the part thickness was measured at ten locations to quantify the amount of cold-work. The cold compression resulted in an average thickness reduction of 3%, which will be referred to as the 3% cold-worked specimen/condition. The non-cold-worked specimen will be referred to as the 0% cold-worked specimen/condition.

Measurements are made on specimens removed from larger forgings with approximate cross-sectional dimensions of 1.1 m (44 in) wide by 686 mm (27 in) tall, and a thickness of 111 mm (4.375 in). The removed specimens are 375 mm (14.75 in) wide, 181 mm (7.125 in) tall, and 111 mm (4.375 in) thick (Figure 1).

The elastic material properties given in [8] were used for all residual stress measurements and consisted of an elastic modulus of 69.6 GPa (10,100 ksi) and a Poisson's ratio of 0.33. The material has a face-centered cubic (FCC) crystal system and material elemental composition that falls within the manufacturer defined specifications (Table 1) [8].

2.2. Residual stress measurements

Residual stress measurements were performed on these two specimens using three different techniques: EDXRD, neutron diffraction, and PSR biaxial mapping. For the sake of comparison, measurements for each different technique were performed on the same specimen, in succession. EDXRD measurements were performed first, ND measurements were performed second, and PSR biaxial mapping measurements were performed last. All of the residual stress measurements were performed along a plane at $z = 0$, which is 76 mm (3 in) from the cut which separated the specimen from the larger forging (Figure 1). The origin of the x-axis is the mid-distance between the two vertical flange centers, the origin of the y-axis is at the mid-thickness of the central web area. The following sections outline the details of the measurement techniques.

2.3. Energy Dispersive X-Ray Diffraction

EDXRD is a polychromatic x-ray diffraction technique capable of capturing the entire diffracted X-ray spectrum at a given diffraction angle [9] used, in this instance, for measuring residual strain in the atomic lattice spacing of polycrystalline metallic materials. The excellent spatial resolution provided by EDXRD is attributable to both the high-brilliance, high-flux X-ray beam, which is dependent upon the X-ray source and the ability to clearly define the beam, which is inherent to the technique through use of incident and diffracted beam slits for respective beam shaping.

The EDXRD measurements were performed at beamline 6-BM-B at the Advanced Photon Source (APS) at the Argonne National Laboratory. Beamline 6-BM-B is dedicated to energy dispersive diffraction using white beam radiation and has a single element Ge detector that is cryogenically cooled. The gauge volume is defined by the incident beam slit width, slit height, and the diffracted angle (0.1 mm, 1 mm, and 7º, respectively). Measurements were made along a rectangular grid between x =

[-51.79 mm, 49.21 mm] in 1.0 mm increments and y = [-11.9 mm, 11.9 mm] in 1.57 mm increments, resulting in 102 measurement grid points along the *x*-direction and 16 measurement grid points along the *y*-direction.

Three strain components are generally required to calculate residual stresses. Typically, measurement of two orthogonal strain components in a plane is relatively straight forward, however, measurement of the third component (normal to the plane defined by the prior two strain components) often cannot be accomplished due to the thickness of the surrounding material. This limitation has restricted the use of X-ray diffraction techniques to either thin components (< 7 mm), where a plane-stress assumption is apparent, or to components whose out-of-plane dimensions do not prohibit the measurement of the third strain component. Due to the geometry of the specimens here, it is not possible to measure all three normal lattice spacing components (i.e., the beam path length for d_{zz} would need to pass through the entire width of the specimen (375 mm), which is beyond the instrument capability). However, for the central web region it is possible to make d_{xx} and d_{yy} lattice spacing measurements (Figure 2). Using these two components of lattice spacing (and strain) along with a plane-stress assumption, it is possible to calculate the full three-dimensional stress state for the region of interest. Preliminary modeling efforts suggest a plane-stress assumption is reasonable. Using the plane stress assumption, stresses were calculated using standard approaches [10] as described below.

The measurements taken here consisted of collecting interatomic lattice spacing data (d) for two orthogonal directions in a specimen containing residual stress and lattice spacing data in a stress-free specimen (d_0). The stress-free (d_0) specimens were made by removing a thin, 2.0 mm wide (0.07 in), 25.4 mm (1.0 in) long, near x = -150 mm. Stress-free specimens were removed from similar specimens for both the 0% and 3% cold-working specimens, so that lattice spacing measurements could be made for both the stressed and stress-free specimens during the specimen experiment. The stress-free comb

had 11 “teeth” that were separated by 2.0 mm (Figure 3). Each comb tooth is assumed to be entirely stress relieved. The lattice spacing was found for the $\{hkl\} = \{311\}$ lattice plane using GSAS [11]. The normal components of the strain tensor were calculated using

$$\varepsilon_{i\{311\}} = \frac{d_{i\{311\}} - d_{0,i\{311\}}}{d_{0,i\{311\}}} \tag{1}$$

where ε_i is the normal strain and $i = x$ or z. The normal components of the stress tensor are then calculated using Hooke’s law:

$$\sigma_{i,\{hkl\}} = \frac{E_{\{hkl\}}}{1+\nu_{\{hkl\}}}\left(\varepsilon_{i,\{hkl\}} + \frac{\nu_{\{hkl\}}}{1-2\nu_{\{hkl\}}}\left(\varepsilon_{x,\{hkl\}} + \varepsilon_{y,\{hkl\}} + \varepsilon_{z,\{hkl\}}\right)\right) \tag{2}$$

where σ_i is the normal stress, $i = x, y,$ or z, ν is Poisson’s ratio, and $E_{\{hkl\}}$ is the elastic modulus for the $\{hkl\}$ plane and taken as the bulk elastic modulus. Due to the consistent face centered cubic (FCC) structure of aluminum, $\{hkl\} = \{311\}$ is used for all EDXRD calculations herein due to its high multiplicity. Enforcement of the plane-stress boundary condition is conducted at this point by first setting $\sigma_{y,\{311\}} = 0$ within Equation 2 and calculating the required $\varepsilon_{y,\{311\}}$ values at every measurement location to satisfy this assumption. The reverse-calculated $\varepsilon_{y,\{311\}}$ values are then used to calculate $\sigma_{x,\{311\}}$ and $\sigma_{z,\{311\}}$ at each measurement location.

Uncertainty was calculated using standard error propagation [12]. The strain uncertainty was assumed to come from two sources. One source was due to a fitting error when determining the lattice spacing, $U\varepsilon_{i,\{hkl\},misfit}$, which was calculated by propagating the lattice spacing fit uncertainty through

$$U\varepsilon^2_{i,\{311\},misfit} = \left(\frac{Ud_{i,\{311\}}}{d_{0,i,\{311\}}}\right)^2 + \left(\frac{d_{i,\{311\}} \cdot Ud_{0,i,\{311\}}}{d^2_{0,i,\{311\}}}\right)^2 \tag{3}$$

where $Ud_{i,\{311\}}$ and $Ud_{0,i,\{311\}}$ are the misfits in the residually stressed and stress free lattice spacings, respectively. The other error incorporated was a baseline instrument uncertainty, $U\varepsilon_{instrument}$, which was taken to be 20 με based on the advice of the instrument scientist. The total strain uncertainty, $U\varepsilon_i$, is found with

$$U\varepsilon_{i,\{311\}}^2 = U\varepsilon_{i,\{311\},misfit}^2 + U\varepsilon_{instrument}^2. \quad (4)$$

The stress uncertainty was found by propagating the strain uncertainty through Equation (2).

$$U\sigma_{i,\{311\}}^2 = \left(\frac{E_{\{311\}}}{1-\nu_{\{311\}}^2}\right)^2 \left(U\varepsilon_{i,\{311\}}^2 + \nu_{\{311\}}^2 U\varepsilon_{j,\{311\}}^2\right) \quad (5)$$

2.4. Neutron diffraction

ND measurements were performed using standard methodologies [10] and recently published guidelines [13]. Neutron diffraction measurements consist of collecting interatomic lattice spacing data (d) in a specimen containing residual stresses and stress-free lattice spacing (d_0) data for three orthogonal directions. The stress-free (d_0) specimens were made by removing a thin slice, 7.6 mm (0.3 in), from similar forgings for both the 0% and 3% cold-worked specimens. The stress-free combs (Figure 4) were cut using wire electric discharge machining (EDM) to a depth of 6.3 mm (0.25 in) with a 10 mm (0.39 in) vertical grid spacing and a 8.9 mm (0.35 in) horizontal spacing.

ND measurements were performed at the VULCAN instrument [14] in the Spallation Neutron Source (SNS) at the Oak Ridge National Laboratory. VULCAN is a time-of-flight instrument with two detector banks at ±90º from the incident neutron beam, allowing for simultaneous lattice spacing measurements in two orthogonal directions (see Figure 5 for measurement diagram). The gage volume used was 5 x 5 x 5 to 10 mm^3. The gage volume was defined by the incident beam slit width, slit height, and the diffracted beam radial collimators (5 mm for all three values). The incident beam slit width and

height was varied when possible so that the gage volume in the z-direction could be increased to 10 mm to reduce measurement collection times. Measurements were made along five horizontal lines at y = [0 mm, ±4.5 mm, ±9 mm] and along six vertical lines at x = [-75 mm, -70 mm, -65 mm, 75 mm, 80 mm, 85 mm] (Figure 6). Measurements in the d_0 specimens were made along three horizontal lines at y = [0 mm, ±9 mm] and along five vertical lines at x = [-80 mm, -70 mm, 60 mm, 70 mm, 80 mm] to be centered at the combs in Figure 4. Point spacing ranged between 5 mm and 20 mm for the horizontal lines and was fixed at 4.5 mm for the vertical lines (Figure 6).

The lattice spacing was found for each $\{hkl\}$ lattice plane using GSAS [15]. The normal components of the strain tensor were calculated using

$$\varepsilon_{i\{hkl\}} = \frac{d_{i,\{hkl\}} - d_{0,i,\{hkl\}}}{d_{0,i,\{hkl\}}} \tag{6}$$

where ε_i is the normal strain (i = [x, y, z]) and $\{hkl\}$ is the given lattice plane. The normal components of the stress tensor are then calculated using Hooke's law (Eq. (2)). Stresses values were calculated using the {311}, {200}, and {220} planes and the results presented here use an average of all three lattice planes, as it was assumed to best represent the bulk stress present in the material. $E_{\{hkl\}}$ and $\nu_{\{hkl\}}$ were taken to be the bulk material properties given above. The uncertainty was calculated using standard error propagation [12] and followed the same approach described above for EDXRD.

2.5. Primary Slice Removal Biaxial Mapping

The primary slice removal (PSR) biaxial mapping measurement uses slitting method measurements in conjunction with the contour method to determine maps of multiple components of residual stress. PSR biaxial mapping uses the superposition principle [16] to decompose the original stress field along a given plane into the stress remaining in a thin slice and the stress that was released when removing the slice (the so-call primary slice removal stress) using

$$\sigma^{original}(x,y) = \sigma^{slice}(x,y) + \sigma^{PSR}(x,y) \quad (7)$$

The PSR biaxial mapping measurements were performed using the methodologies described in [17,18].

The x and y-direction stress remaining in the slice, σ^{slice}, was mapped using a series of slitting method measurements. The slitting measurements were made in two 7.3 mm (0.3 in) thick slices using the approach given in [19]. The measurements consisted of placing a strain gage on the opposite side of the slitting cut path and recording the strain change during a series of incremental slit depths. A total of 28 slitting measurements were performed, where 25 measurements were used to calculate σ_{xx}^{slice} and 3 measurements were used to find σ_{yy}^{slice}. The measurement locations can be seen in Figure 7.

The measured strain versus depth was used to calculate stress using an elastic inverse [20], which incorporated Tikhonov regularization [21] to reduce the effect of noise. The stress calculation also used the finite slice thickness correction developed by Aydıner and Prime [22]. The uncertainty in the slitting measurements was calculated using the difference between the smoothed strain and measured strain (or alternately with an assumed, omnipresent value of 2 με) in the stress calculation procedure. The slitting uncertainty did not include an uncertainty arising from fitting the data inappropriately (i.e., a "model error" uncertainty [23]) because an uncertainty estimate for this type of error has not been developed for unit pulse basis functions.

The primary slice removal stress, σ^{PSR}, is the stress change that occurs when the slice is parted from the specimen. Previous work [17, 24] has shown that this stress change can be computed using the out-of-plane stress (σ_{zz}) that was initially present on cut faces of the slice when it was part of the larger body. The out-of-plane stress is measured with the contour method following the approach given in [25]. The forging was sectioned along the measurement plane with a wire EDM. Prior to

sectioning, the specimen was rigidly clamped to the EDM frame and allowed to come to thermal equilibrium with the cutting fluid. After sectioning, the surface height profile of each resulting cut surface (two per cut) was measured as a function of in-plane position with a scanning profilometer. A measurement spacing of 500 μm was used for the surface scans, resulting in roughly 100,000 points per surface. The two cut surface profiles were then averaged and fitted with an analytical smoothing function. The residual stress was calculated using a linearly elastic finite element model of the cut specimen. The finite element analysis consisted of applying the negative of the smoothed surface profile as a displacement boundary condition to the cut face of the specimen. The finite element model used commercial software (ABAQUS) with eight-node linear brick elements (C3D8), and the elastic material properties given above.

To determine σ^{PSR}, a finite element model of the slice was used. The σ_{zz} stress from the contour measurement was applied as a traction boundary condition to each face of the slice model. The slice model also used eight-node linear brick elements (C3D8) and the material properties given above. The model had a node spacing of approximately 1 node per mm and six nodes through the slice half-thickness. The resulting equilibrated stress field provides σ^{PSR}.

All uncertainty in σ^{PSR} is assumed due to uncertainty in σ_{zz} measured using the contour method. Uncertainty in the out-of-plane component of σ^{PSR} (σ_{zz}) was determined using an uncertainty estimator described earlier [26]. Uncertainty in the in-plane components of σ^{PSR} (σ_{xx} and σ_{yy}) was assumed to be negligible based on prior work [17], where it was found that the smooth out-of-plane stress field causes an in-plane stress field robust to small-scale, random variations in the out-of-plane stress. As a result, uncertainty in total in-plane stress components derives entirely from uncertainty in the slitting measurements and uncertainty in the total out-of-plane stress component derives entirely from uncertainty in the contour measurement.

3. RESULTS

Two-dimensional stress and uncertainty maps for both the 0% and 3% cold-worked specimens can be seen in Figure 8 through Figure 13. Each figure shows the measured stress and uncertainty, when applicable, for EDXRD, ND, and PSR biaxial mapping.

The results from all techniques for σ_{xx} in the 0% cold-working condition (Figure 8) show compressive stress (minimum near -200 MPa) along the exterior of the specimen and tensile stresses toward the specimen center-line (maximum near 130 MPa). The stress magnitudes found for all three measurement technique are in general agreement. The uncertainty is nominally constant over the cross-section for each measurement, with EDXRD, ND, and PSR biaxial mapping having uncertainty around 15 MPa, 20 MPa, and 5 MPa, respectively. However, there are larger uncertainties for all three measurements at localized regions; especially towards the flange at 50 mm for the EDXRD measurements (25 MPa), the interior of the flanges for ND (25 MPa), and around x = 130 mm for PSR biaxial mapping (25 MPa).

For EDXRD and PSR biaxial mapping, results for σ_{xx} in the 3% cold-worked condition (Figure 9) are very similar to the trends from the 0% cold-worked condition, only with smaller magnitudes. The minimum compressive stress along the specimen exterior was near -50 MPa while the tensile stress maximum is near 80 MPa, toward the specimen center-line. The EDXRD and PSR biaxial mapping results are in nominal agreement, while the ND measurement shows significant disagreement where the stress is nominally compressive (minimum near -100 MPa) or near zero over the central web region. The uncertainty has similar values as for the 0% cold-worked condition, but for each measurement there is a local region of larger uncertainty (up to 40 MPa, 50 MPa, and 50 MPa for the EDXRD, ND, and PSR biaxial mapping techniques, respectively).

The results for σ_{yy} in the 0% cold-working condition (Figure 10) show that the stresses found with PSR biaxial mapping and ND are in nominal agreement. Near the specimen center-line, ND found low magnitude stress over most of the cross-section, but larger tensile stress near each of the flanges (near $x = \pm 75$ mm). The ND uncertainty is very similar to that found in the σ_{xx} 0% cold-working measurements (20 MPa over most the cross-section with uncertainties near 25 MPa in the flanges). The PSR biaxial mapping uncertainties are around 5 MPa over most of the measurement area with a localized region of higher uncertainty (35 MPa) at $x = 65$ mm.

The results for σ_{yy} in the 3% cold-working condition (Figure 11) shows that the stresses have been significantly reduced to lower magnitudes (±30 MPa) at most points. The ND and PSR biaxial mapping results are in nominal agreement. The uncertainty for ND has a nearly identical distribution to the σ_{xx} 3% cold-working condition (20 MPa over most the cross-section with uncertainties near 25 MPa in the flanges). The PSR biaxial mapping uncertainties are very similar to the uncertainty found in the 0% cold working condition and are around 5 MPa over most of the measurement area with a localized region of higher uncertainty at $x = 65$ mm (35 MPa).

The results for σ_{zz} in the 0% cold-working condition (Figure 12) show that there is excellent agreement between all measurement techniques, with maximum compressive stress (minimum near -300 MPa) along the exterior of the specimen and maximum tensile stresses toward the specimen center-line (maximum near 250 MPa). The compressive magnitudes found with EDXRD are somewhat larger than those in other measurements. The uncertainty is nearly constant over the cross-section for each measurement, with EDXRD, ND, and PSR biaxial mapping having uncertainty around 15 MPa, 20 MPa, and 30 MPa, respectively.

The results for σ_{zz} in the 3% cold-working condition (Figure 13) show similar trends to the 0% cold-working condition, only with smaller stress magnitudes. The compressive stress has a maximum around

-100 MPa along the specimen exterior and tensile stresses with a maximum near 80 MPa toward the specimen center line. The EDXRD and PSR biaxial mapping results are similar, however, the ND results have significant differences relative to the other techniques (as was the case for the other stress components). The uncertainty has similar values to the 0% cold-working condition for EDXRD and ND, with a localized region of larger uncertainty (30 MPa) near x = -50 mm for EDXRD and toward the center-line inside the flanges for ND. The uncertainty for the PSR biaxial mapping measurement was significantly lower at 10 MPa.

Line plots of the stress at $x = 0$ and along the specimen center line ($y = 0$) are shown in Figure 14 through Figure 18 for each condition. The results for σ_{xx} at $x = 0$ show similar trends between the methods for the 0% cold-worked condition (Figure 14a). The EDXRD stresses appear to be roughly 50 MPa lower than ND and PSR biaxial mapping results at most locations. The results for σ_{xx} at x = 0 in the 3% cold working condition (Figure 14b) show excellent agreement between the EDXRD and PSR biaxial mapping, but the ND results are different and will be further discussed below. The results for σ_{xx} along the center line show good agreement for the 0% cold-worked condition (Figure 15a) for the central portion of the forgings ($x = \pm 50$ mm). Outside of that region there are similar trends between the measurements, but with significantly different magnitudes. For the 3% cold-working condition (Figure 15b), there is good agreement between the EDXRD and PSR biaxial mapping measurements, but the ND results are different (as was the case at x = 0).

The σ_{yy} results along the center line show good agreement for the 0% cold-working condition (Figure 16a) for all x values, however, the PSR biaxial mapping results have somewhat larger stress from $75 < x < 110$ mm. The 3% cold-worked condition (Figure 16b), shows excellent agreement between the ND and PSR biaxial mapping measurements.

The results for σ_{zz} at $x = 0$ show similar trends between the methods for the 0% cold-worked condition (Figure 17a). The EDXRD stresses appear to be roughly 50 MPa lower than ND and PSR biaxial mapping results at locations near the perimeter. The σ_{zz} results show a very similar stress profile to the σ_{xx} results, with the σ_{zz} results show slight smaller stresses. The results for σ_{zz} at $x = 0$ in the 3% cold working condition (Figure 17b) show good agreement between the ND and PSR biaxial mapping (except at $y = 0$). The EDXRD results show a similar trend to the ND and PSR biaxial mapping results, but the stress values are approximately 50 MPa lower at most locations. The σ_{zz} results along the center line show good agreement for the 0% cold-working condition (Figure 18a) for $x < 50$ mm. For the 3% cold-working condition (Figure 18b), there is good agreement between EDXRD, PSR biaxial mapping, and ND for $-50 < x < 50$ mm.

4. DISCUSSION

The measured results illustrate the ability of cold working to reduce the level of residual stress in aluminum die forgings. To show the effectiveness of the stress mitigation technique, histograms for σ_{zz} in the 0% and 3% cold working conditions are shown in Figure 19 (at all measurement locations). The dispersion in the residual stress data (on both the tensile and compressive extremes) is significantly reduced in the 3% cold working condition relative to the 0% cold working condition. The histograms for all three stress components show similar trends, but the stress magnitude reduction is significant for both the σ_{xx} and σ_{zz} stresses, but somewhat muted for the σ_{yy} stress (not shown for brevity).

The change in residual stress due to cold working (difference between the results for the 3% cold-working condition minus the 0% cold-working condition) is shown in Figure 20 for σ_{xx} and σ_{zz} for all measurement techniques. Both EDXRD and PSR biaxial mapping show the stress change for the σ_{xx} stress to be tensile toward the part perimeter (maximum near 75 MPa) and compressive near the centerline (minimum near -30 MPa), which indicates smaller stress magnitudes in the 3% cold working

condition than in the 0% cold working condition. The σ_{xx} stress change found for ND shows high magnitude compressive stress (-150 MPa) for $y < \pm 17$ mm, which may suggest something problematic is occurring in the measurements in one or both of the specimens. The stress difference for σ_{zz} shows excellent agreement between all three measurement methods, with all showing an "x" shaped distribution with tensile stress towards the exterior corners of the web region (maximum near 150 MPa) and low magnitude compressive stress towards the center (minimum near -25 MPa). The poor agreement (differing stress magnitudes and large uncertainty) between the ND results and other techniques for σ_{xx}, but good agreement for the σ_{zz} component is confounding. One potential explanation for this discrepancy is the larger influence cold working has on crystallographic texture in thick regions that are immediately adjacent to die contact points (i.e. - experience the largest amounts of material flow). This potential for large texture disruption can have a negative effect on diffraction based measurements, particularly if large gage volumes are used, as was the case for the ND experiment here.

Overall, the measurements demonstrate good agreement between EDXRD and PSR biaxial mapping, and some agreement with the ND results, while also highlighting the strengths and limitations of each technique. EDXRD measurements, as implemented here, are capable of very large spatial measurement densities but are limited to measurement areas where a plane-stress assumption yields a reasonable approximation of the actual stress field. ND measurements can map all three normal stress components in a much greater range of thicknesses but can potentially be problematic for measurement locations with preferentially oriented grains (i.e., highly textured specimens). PSR biaxial mapping allows for measurements of stress in one or two directions (beyond a typical contour method measurement) and has low measurement uncertainty but is limited by the number of slitting measurements that can be done within a reasonable time or budget.

The use of EDXRD required a plane-stress assumption in this case since the path length to measure d_{zz} would be prohibitively long. The fact that there is reasonable agreement between PSR biaxial mapping and EDXRD results (based on a plane-stress assumption) may support the validity of the plane-stress assumption for this case. However, as the EDXRD measurements approach the flange regions the plane stress assumption may not be valid and is likely the cause of the small discrepancies between the measurements near $x = \pm 55$ mm.

Un-textured materials (grain orientation is heterogeneous) work well for diffraction experiments as they contain a sufficient number of grains oriented such that the incident beam will diffract from a crystallographic plane of interest. This allows for sufficient diffracted beam flux (i.e., number of particles diffracted) to take measurements along a chosen measurement plane. Highly-textured materials (grains have preferential orientation) are much more difficult to measure as they will only diffract particles for very specific work piece alignments, potentially preventing measurements at a desired location [27]. The cold-working process increases texture local to die-contacted regions and could explain the outlying neutron diffraction measurements in the 3% cold working condition as well as the increase in uncertainty for the 3% cold working diffraction measurements. Although the average part thickness reduction is 3% for the 3% cold working condition, localized strain is likely to be significantly larger at the surfaces where die-contact occurs. To assess whether grain size or texture differences were present between the 0% and 3% cold working conditions, the ratio of peak intensities from different lattice planes during the neutron diffraction experiments on the 0% and 3% were compared. Figure 21 shows the ratio of the {200} and {220} lattice plane peak intensity relative to the {311} lattice plane. The results along the specimens centerline at $y = 0$ show that the 3% lattice plane has significantly higher peak intensity ratios for d_x and d_z, whereas they are roughly similar for d_y. Constant peak intensity ratios would be expected between the specimens if the texture and grain size were consistent between specimens, but they were found to be significantly different here, indicating that significant

texture or grain size differences could be present and may be causing the neutron diffraction results to not agree with those from those the other two techniques in the 3% cold working condition.

The significant difference in the PSR uncertainty for σ_{zz} (10-30 MPa) and for the in-plane stress components (roughly 5 MPa) is due to precision of the underlying experimental techniques. As stated above, uncertainty in σ_{zz} derives from uncertainty in the contour measurement, whereas uncertainty in σ_{xx} and σ_{yy} derives mainly from the slitting measurements. A contour method repeatability study in quenched aluminum found precision (repeatability standard deviation) of 20 MPa near the boundaries of the measurement plane and 5 to 10 MPa in the plane interior [28]. A slitting method repeatability study in laser peened stainless steel specimens found precision (repeatability standard deviation) of 15 MPa (about 2% of stress range) [29]; when scaled by elastic modulus, expected precision in aluminum would be 5 MPa. These prior studies suggest that slitting has better precision than contour, and are consistent with the fact that the present uncertainty in σ_{zz} is larger than uncertainties in σ_{xx} and σ_{yy}. The prior studies also report levels of precision that are consistent with the uncertainties reported here. Even so, the level of uncertainties for in-plane stress components is rather small, and would be larger if the uncertainty estimates included a contribution from model error. Note that the relatively homogenous spatial distribution in uncertainty for σ_{zz} is caused by the introduction of a floor to the contour method uncertainty estimate [26]. The uncertainty for σ_{zz} is significantly larger for the high-stress condition (about 30 MPa) than for the low-stress condition (about 10 MPa) which is due to the high-stress surface profile being difficult to fit, and the fit being more uncertain. Some localized regions of high uncertainty in in-plane stress (near x = 110 mm in Figure 8 and Figure 9 and near y = 0 in Figure 10 and Figure 11) are caused by individual slitting measurements that had somewhat ill-suited geometry, where the capacity of the strain gage to measure released strain was impaired [30].

Another important influence in diffraction based experiments, beyond access prohibitively long path lengths and texture, is gage volume dimensions. The selection of an appropriate gage volume is determined by a variety of factors (e.g., grain size, experimental setup, type of particle, flux of the particle source, gradient of residual stress field, and required diffracted beam strength). ND measurements made in the 0% cold-worked article correlated very well to the rest of the techniques used at the centerline of the article, however, the correlation of the ND measurements near the surface is poor. This may be a direct result of the large gage volume dimensions used: the centerline residual stresses are symmetric about the centerline and, when averaged, yields a representative value for the region. However, when the large gage volume is used near the surface, the non-symmetric gradient averages into a stress value that is less representative for that region. Furthermore, it is possible that the neutron diffraction gage volume encountered the edge of the specimens due to beam divergence and could cause an "edge effect" error (the distance between the top of the gage volume and the edge of the specimen is 0.5 mm.

Another factor that could contribute to the results in the diffraction based experiments (and the differences observed between the measurement techniques) was the decision to use the bulk material properties rather than material properties that are specific to each $\{hkl\}$ lattice plane or spatially varying material properties (which are driven by local texture).

5. SUMMARY/CONCLUSIONS

A series of residual stress measurements were made on two 7085 die forgings (with and without cold working stress relief). This work provides a comparison of two particle diffraction measurement techniques (EDXRD executed at APS and ND conducted Oak Ridge National Laboratory) alongside a new strain-release technique (PSR biaxial mapping). The results showed good agreement between the methods for the 0% cold working condition and good agreement between EDXRD and PSR biaxial

mapping for the 3% cold working condition. These measurements show that it is possible to measure bulk residual stresses using a range of techniques in aluminum die forgings. Having demonstrated a variety of useful measurements allows for flexibility for future measurements in similar conditions. The measurements demonstrated that cold working aluminum die forgings effectively reduces residual stress magnitudes.

Both the diffraction measurements are limited by the availability of appropriate X-ray or neutron sources, which are high-energy radiation sources or a large flux neutron source for through-thickness transmission type measurements. The PSR biaxial mapping measurement is commercially available.

6. ACKNOWLEDGEMENTS

The authors acknowledge, with gratitude, the U.S. Air Force for providing financial support for this work (contract FA8650- 14-C-5026). We would also like to acknowledge Jun-Sang Park and John Okasinski from Argonne National Laboratory for their help with the energy dispersive x-ray diffraction measurement data collection and analysis, Ke An and Matthew Frost from Oak Ridge National Laboratory for their help with the neutron diffraction measurement.

This research used resources of the Advanced Photon Source, a U.S. Department of Energy (DOE) Office of Science User Facility operated for the DOE Office of Science by Argonne National Laboratory under Contract No. DE-AC02-06CH11357. A portion of this research at ORNL's Spallation Neutron Source was sponsored by the Scientific User Facilities Division, Office of Basic Energy Sciences, US Department of Energy.

REFERENCES

[1] Sim WM, "Challenges of residual stress and part distortion in the civil airframe industry. *Int J Microstructure and Materials Properties*, 5(4/5):446–455, 2010

[2] D. L. Ball, M. J., R. J. Bucci, J. Watton, A. T. DeWald, M. R. Hill, C. F. Popelar, and R. McClung. "The Impact of Forging Residual Stress on Fatigue in Aluminum", *56th AIAA/ASCE/AHS/ASC Structures, Structural Dynamics, and Materials Conference, AIAA SciTech Forum*, (AIAA 2015-0386)

[3] B. Cowles, D. Backman, and R. Dutton, "Verification and validation of ICME methods and models for aerospace applications," *Integrating Materials*, vol. 1, no. 1, p. 2, 2012.

[4] B. A. Cowles, L. Cowles Consulting, C. T. Tolland, D. G. Backman, and R. E. Dutton, "The Development and Implementation of Integrated Computational Materials Engineering (ICME) for Aerospace Applications," *Models, Databases and Simulation Tools Needed for Realization of Integrated Computational Materials. Engineering, Proceedings of the Symposium Held at Materials Science & Technology, 2010*,.

[5] B. A. Cowles, D. G. Backman, and R. E. Dutton, "Update to recommended best practice for verification and validation of ICME methods and models for aerospace applications," *Integrating Materials and Manufacturing Innovation*, vol. 4, no. 1, p. 2, 2015.

[6] D. L. Ball *et al.*, "A Detailed Evaluation of the Effects of Bulk Residual Stress on Fatigue in Aluminum," in *Advanced Materials Research*, 2014, vol. 891, pp. 1205–1211.

[7] SAE Aerospace, "Aerospace Material Specification 4403: Aluminum Alloy, Die Forgings, Solution Heat Treated, Compression Stress-Relieved, and Overaged," 2006.

[8] Mueller L., Suffredini L., Bush D., Sawtell R., Brouwer P., "Alcoa 7085 Die Forgings Green Letter," ALCOA, 2006.

[9] A. Steuwer, J. R. Santisteban, M. Turski, P. J. Withers, and T. Buslaps, "High-resolution strain mapping in bulk samples using full-profile analysis of energy-dispersive synchrotron X-ray diffraction data," *J. Appl. Crystallogr.*, vol. 37, no. 6, pp. 883–889, Dec. 2004.

[10] ISO, "Non-destructive testing - Standard test method for determining residual stresses by neutron diffraction," International Organization for Standardization, ISO/TS 21432, 2005.

[11] A. C. Larson and R. B. Von Dreele, "General Structural Analysis System (GSAS)," Los Alamos National Laboratory Report LAUR 86-748, 2004.

[12] H. W. Coleman and W. G. Steele, in *Experimentation, Validation, and Uncertainty Analysis for Engineers*, 3rd ed., Hoboken, New Jersey: John Wiley & Sons, Inc., 2009.

[13] A. D. Krawitz, "Neutron Strain measurement," Mater. Sci. Technol., vol. 27, no. 3, pp. 589–603, 2011.

[14] X. L. Wang et al., "VULCAN—The engineering diffractometer at the SNS," Physica B Condens. Matter, vol. 385–386, Part 1, pp. 673–675, Nov. 2006.

[15] A. C. Larson and R. B. Von Dreele, "General Structural Analysis System (GSAS)," Los Alamos National Laboratory Report LAUR 86-748, 2004.

[16] H. F. Bueckner, "The propagation of cracks and the energy of elastic deformation," *Transactions of the American Society of Mechanical Engineers*, vol. 80, pp. 1225–1230, 1958.

[17] M. D. Olson and M. R. Hill, "A New Mechanical Method for Biaxial Residual Stress Mapping," *Exp. Mech.*, vol. 55, no. 6, pp. 1139–1150, 2015.

[18] M. D. Olson, J. S. Robinson, R. C. Wimpory, and M. R. Hill, "Characterisation of residual stresses in heat treated, high strength aluminium alloy extrusions," *Mater. Sci. Technol.*, vol. 32, no. 14, pp. 1427–1438, 2016.

[19] M. R. Hill, "The Slitting Method," in Practical Residual Stress Measurement Methods, G. S. Schajer, Ed. West Sussex, UK: John Wiley & Sons, 2013, pp. 89–108.

[20] M. B. Prime, "Experimental procedure for crack compliance (slitting) measurements of residual stress," Los Alamos National Laboratory, Engineering Sciences and Applications Division, Prime, LA-UR-03-8629, 2003.

[21] G. S. Schajer and M. B. Prime, "Use of Inverse Solutions for Residual Stress Measurements," J. Eng. Mater. Technol., vol. 128, no. 3, pp. 375–382, Jul. 2006.

[22] C. C. Aydıner and M. B. Prime, "Three-Dimensional Constraint Effects on the Slitting Method for Measuring Residual Stress," J. Eng. Mater. Technol., vol. 135, no. 3, p. 031006, May 2013.

[23] M. B. Prime and M. R. Hill, "Uncertainty, Model Error, and Order Selection for Series-Expanded, Residual-Stress Inverse Solutions," *J. Eng. Mater. Technol.*, vol. 128, no. 2, pp. 175–185, Apr. 2006.

[24] M. R. Hill, M. D. Olson, and A. T. DeWald, "Biaxial Residual Stress Mapping for a Dissimilar Metal Welded Nozzle," in ASME 2014 Pressure Vessels & Piping Division Conference, 2014.

[25] M. B. Prime and A. T. DeWald, "The Contour Method," in Practical Residual Stress Measurement Methods, G. S. Schajer, Ed. West Sussex, UK: John Wiley & Sons, Ltd, 2013, pp. 109–138.

[26] M. D. Olson, A. T. DeWald, M. R. Hill, and M. B. Prime, "Estimation of Uncertainty for Contour Method Residual Stress Measurements," *Exp. Mech.*, vol. 55, no. 3, pp. 577–585, 2014.

[27] Y. D. Wang, R. L. Peng, and R. McGreevy, "High anisotropy of orientation dependent residual stress in austenite of cold rolled stainless steel," *Scr. Mater.*, vol. 41, no. 9, pp. 995–1000, Oct. 1999.

[28] M. R. Hill and M. D. Olson, "Repeatability of the Contour Method for Residual Stress Measurement," *Exp. Mech.*, vol. 54, no. 7, pp. 1269–1277, Sep. 2014.

[29] M. J. Lee and M. R. Hill, "Intralaboratory Repeatability of Residual Stress Determined by the Slitting Method," *Exp. Mech.*, vol. 47, no. 6, pp. 745–752, Dec. 2007.

[30] M. D. Olson, M. R. Hill, J. S. Robinson, A. T. DeWald, and V. Sloan, "Residual Stress Mapping with Multiple Slitting Measurements," in *SEM 2015 Annual Conference and Exposition on Experimental and Applied Mechanics*, 2015.

TABLES

Al	Cu	Mg	Zr	Zn
89.8	1.6	1.5	0.1	7

Table 1: Material composition (in weight %)

FIGURES

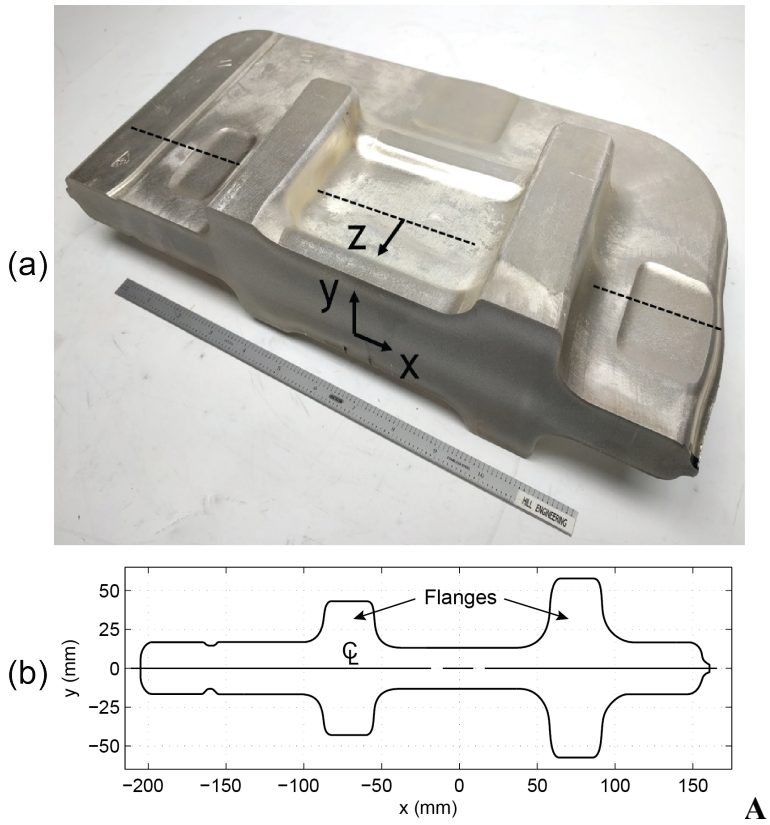

Figure 1: 7085 aluminum forging specimen with dimensions of 375 mm (14.75 in) wide, 181 mm (7.125 in) tall, and 111 mm (4.375 in) thick. The measurement plane is 76 mm (3 in) from the prior cut face, at z = 0 (shown as a dashed line).

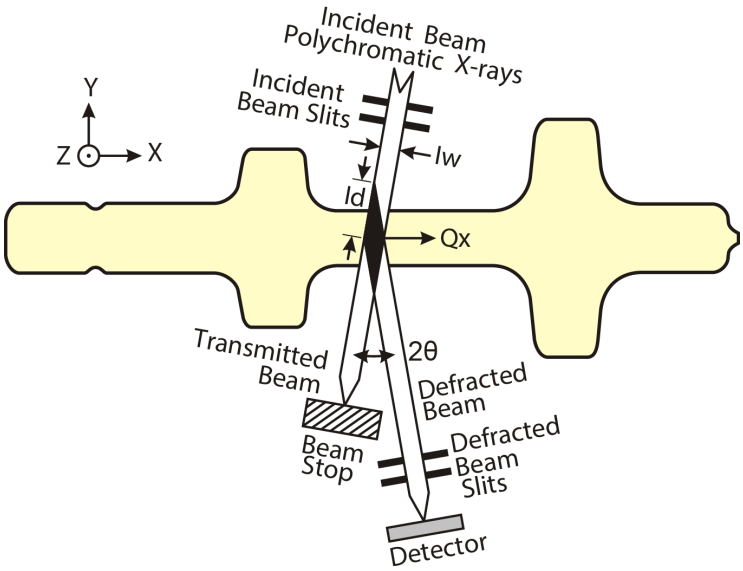

Figure 2: Setup for a generic energy dispersive X-ray diffraction experiment (EDXRD). Qx is the direction vector for strain measurement (in the x-direction), Iw is the incident beam width, Id is the interrogated volume depth, and θ is the diffraction angle set for the experiment. Note: gage volume is not drawn to scale.

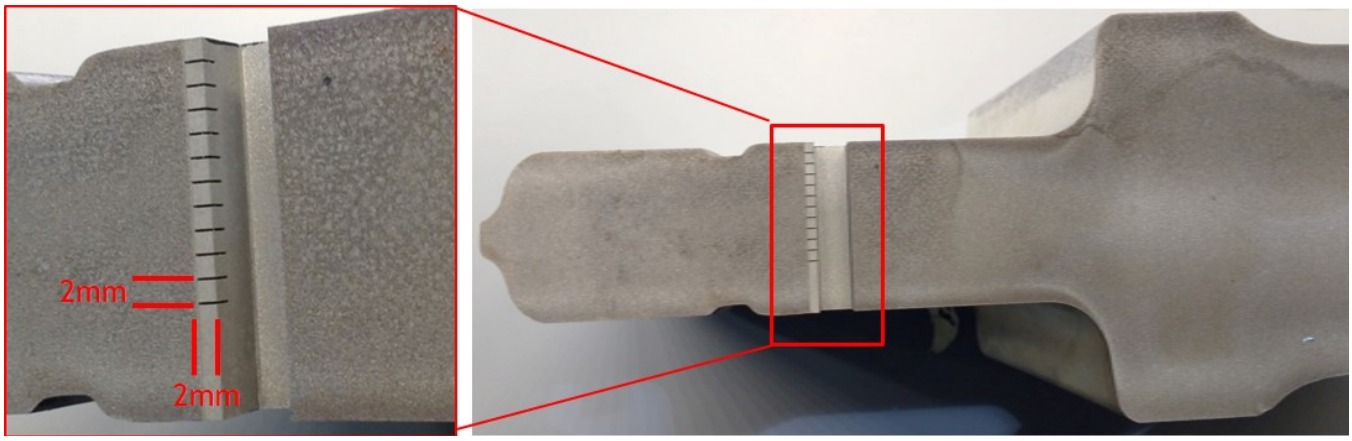

Figure 3: 7085 aluminum die forging stress-free (d_0) specimen used for EDXRD; Detail: comb placed in region of removal with strain relieved region dimensions.

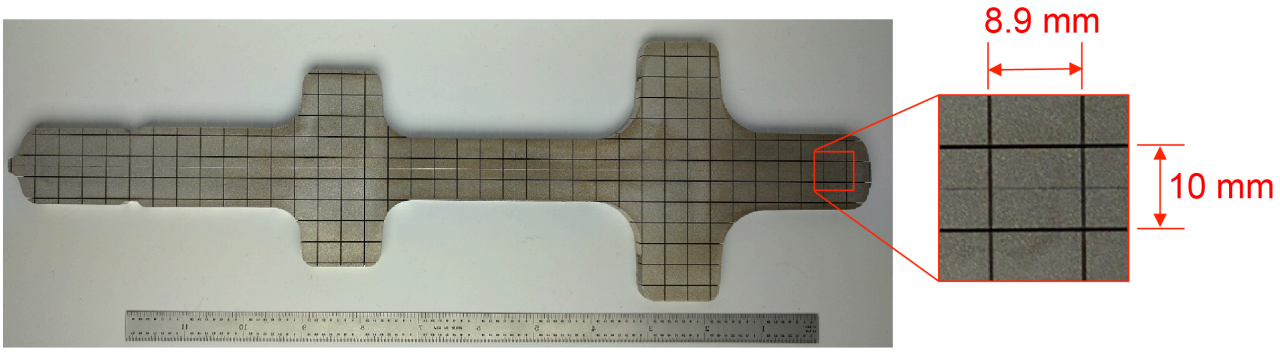

Figure 4: 7085 aluminum die forging stress-free (d_0) specimen used for ND.

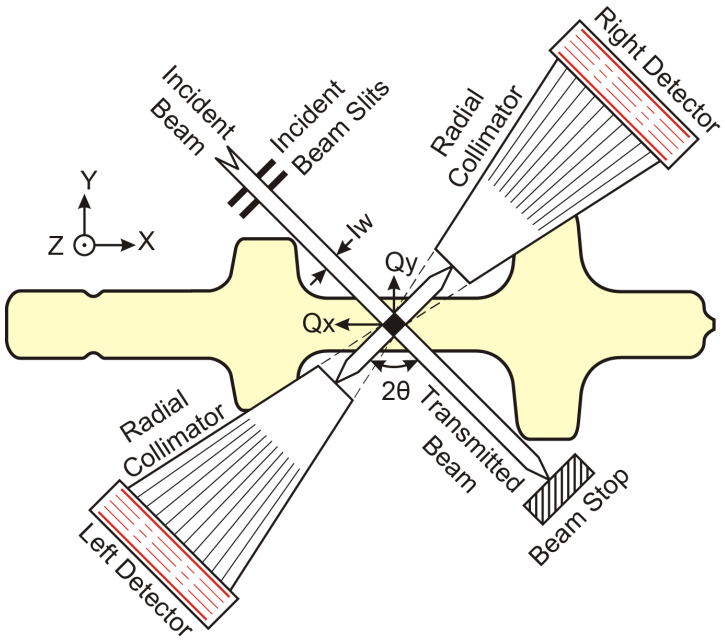

Figure 5: Setup for a generic neutron diffraction experiment. Q is the direction vector for strain measurements (Qx and Qy in the x and y-directions, respectively), Iw is the incident beam width, and θ is the diffraction angle set for the experiment.

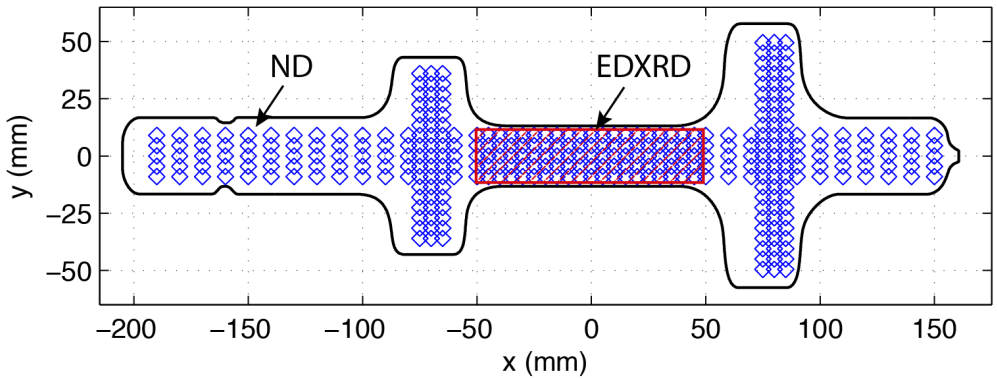

Figure 6: EDXRD and neutron diffraction measurement locations.

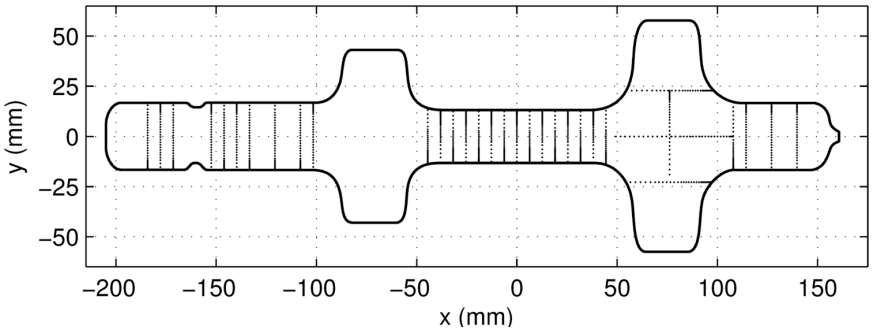

Figure 7: Slitting measurement locations for the PSR biaxial mapping measurement. A total of 33 slitting measurements are used to define the 2D map.

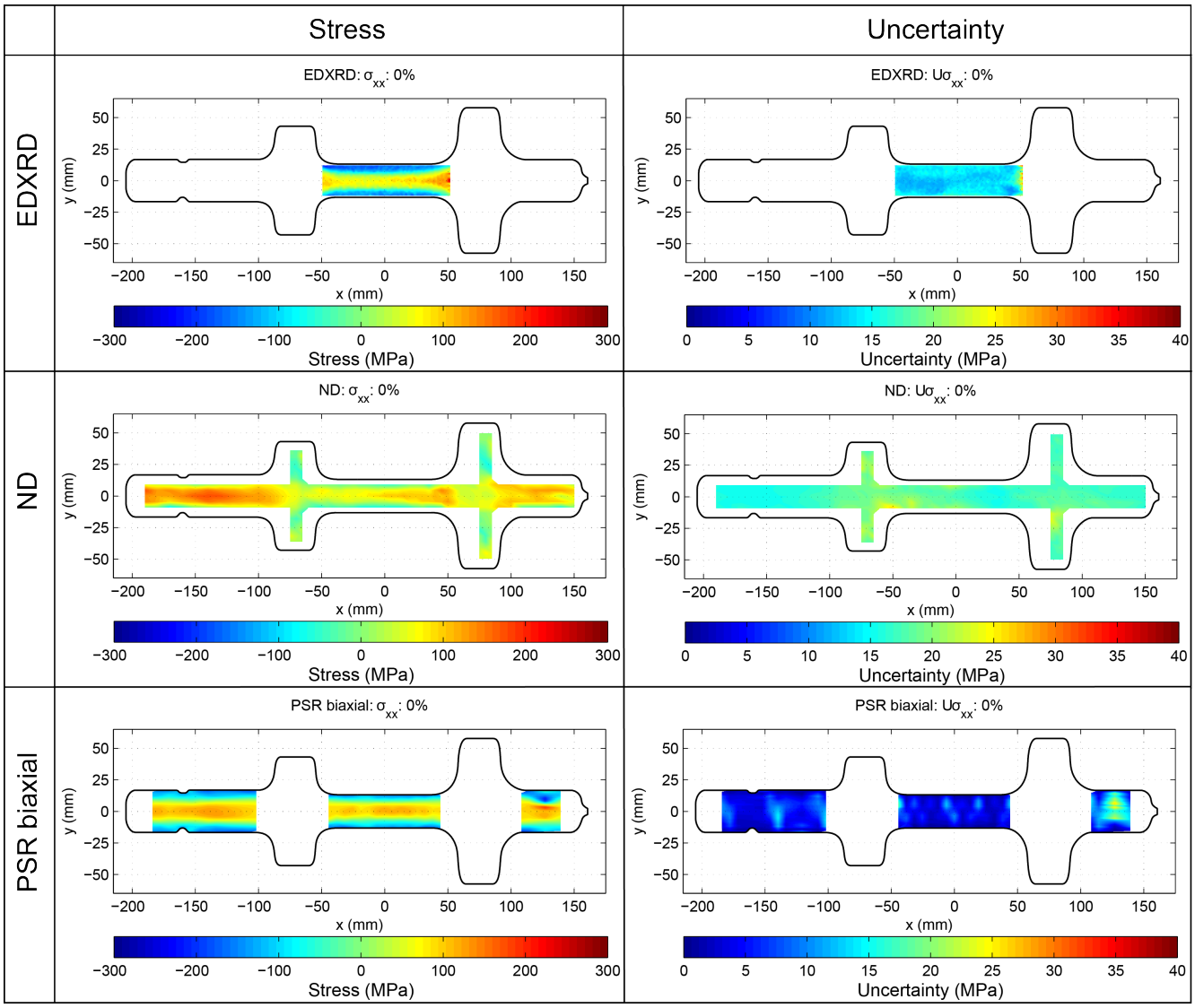

Figure 8: Measured stress and uncertainty (σ_{xx}) for the 0% cold-working condition. Top row is energy disspersive x-ray diffraction (EDXRD), second row is neutron diffraction (ND), and the third row is the Primary slice removal biaxial mapping (PSR). The left column is the stress and the right column is the uncertainty.

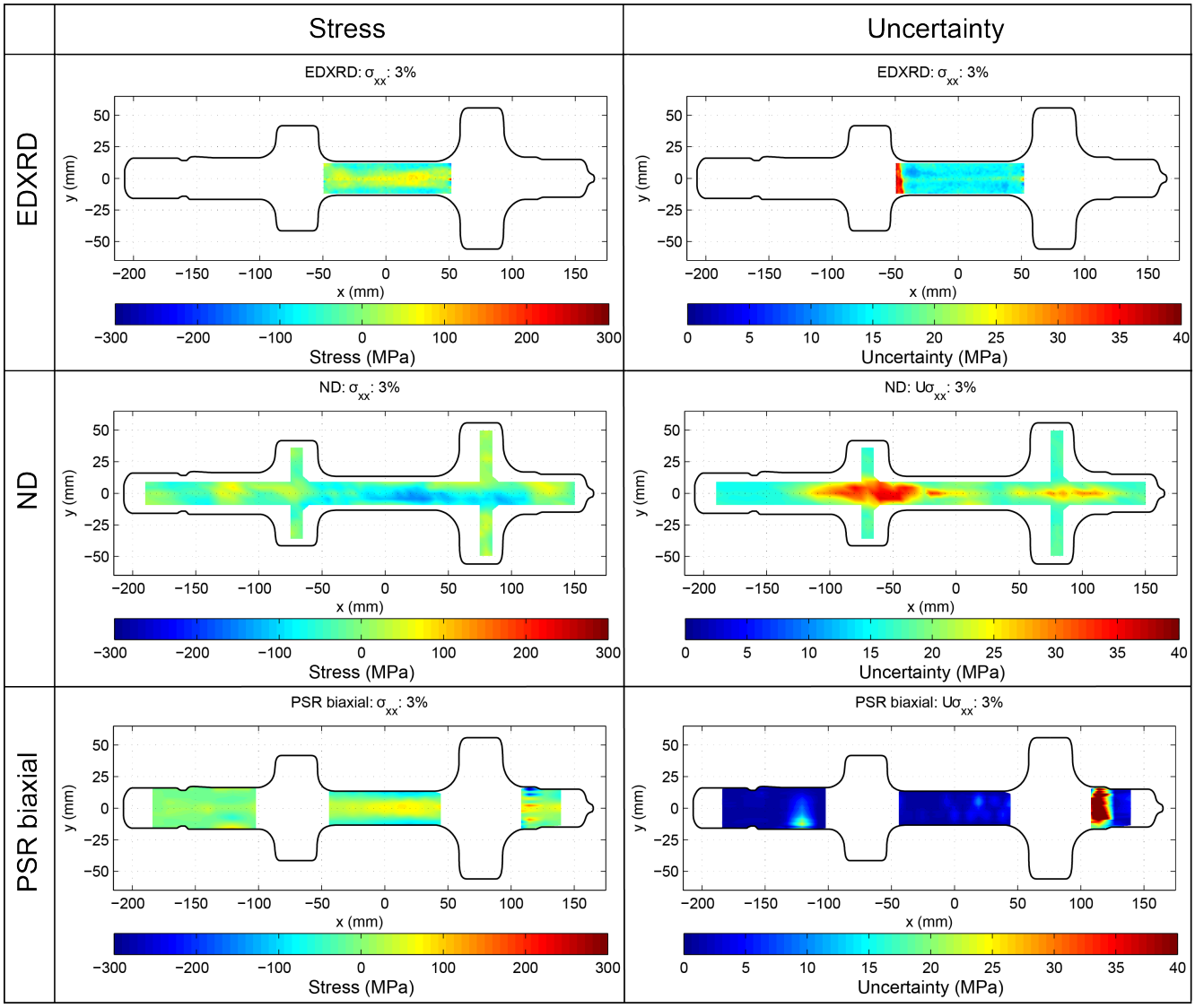

Figure 9: Measured stress and uncertainty (σ_{xx}) for the 3% cold-working condition. Top row is energy disspersive x-ray diffraction (EDXRD), second row is neutron diffraction (ND), and the third row is the Primary slice removal biaxial mapping (PSR). The left column is the stress and the right column is the uncertainty.

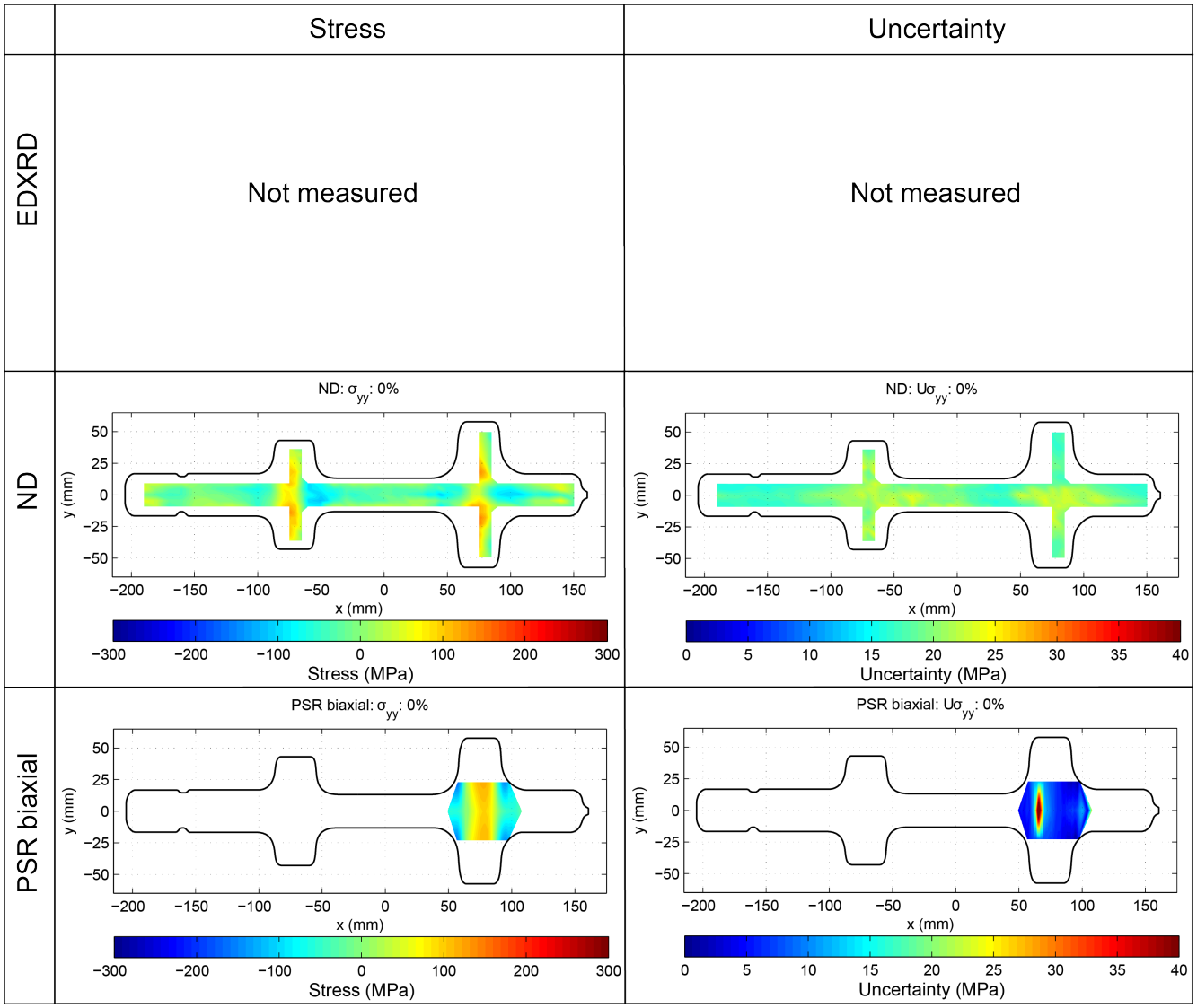

Figure 10: Measured stress and uncertainty (σ_{yy}) for the 0% cold-working condition. Top row is energy disspersive x-ray diffraction (EDXRD), second row is neutron diffraction (ND), and the third row is the Primary slice removal biaxial mapping (PSR). The left column is the stress and the right column is the uncertainty.

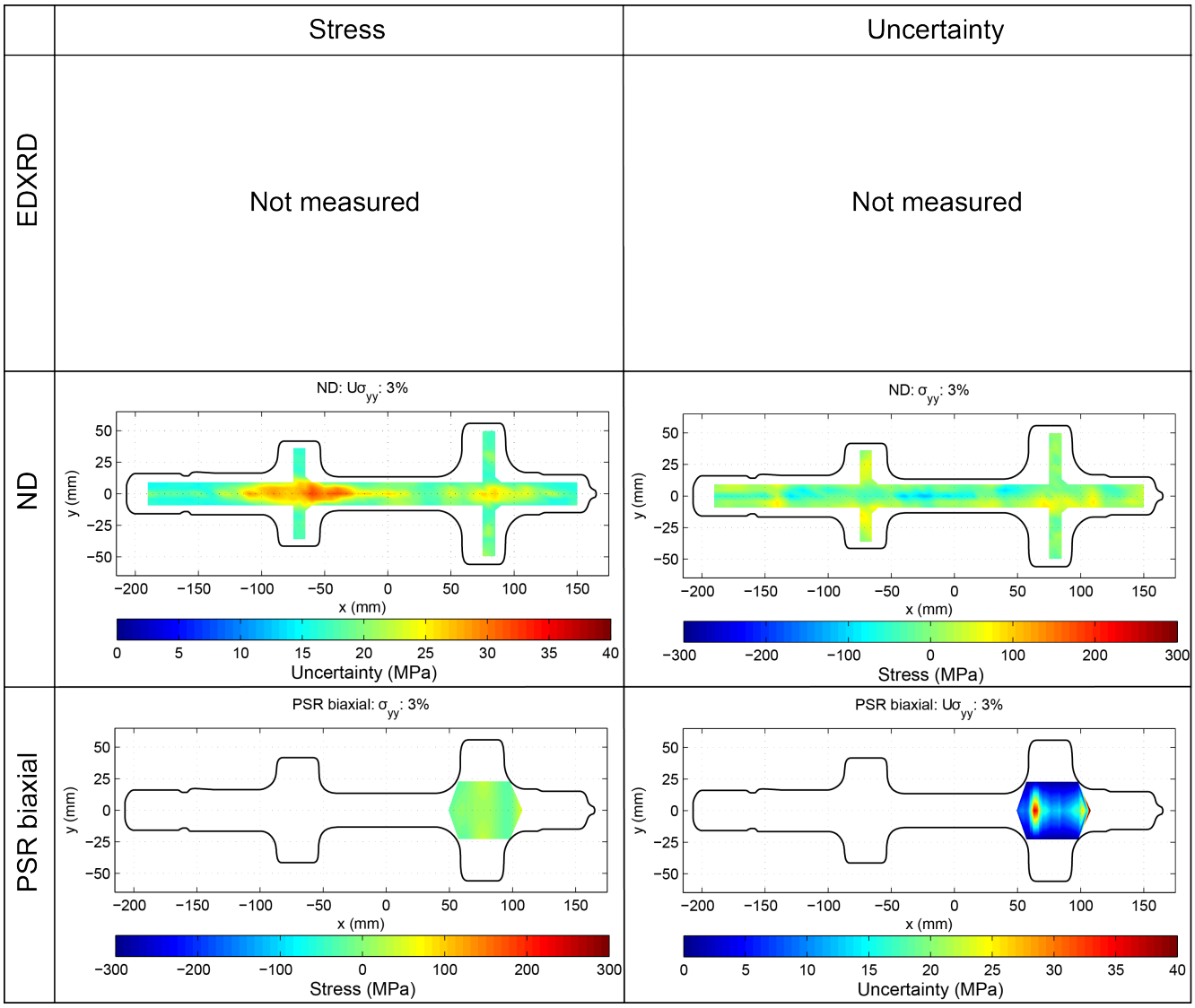

Figure 11: Measured stress and uncertainty (σ_{yy}) for the 3% cold-working condition. Top row is energy disspersive x-ray diffraction (EDXRD), second row is neutron diffraction (ND), and the third row is the Primary slice removal biaxial mapping (PSR). The left column is the stress and the right column is the uncertainty.

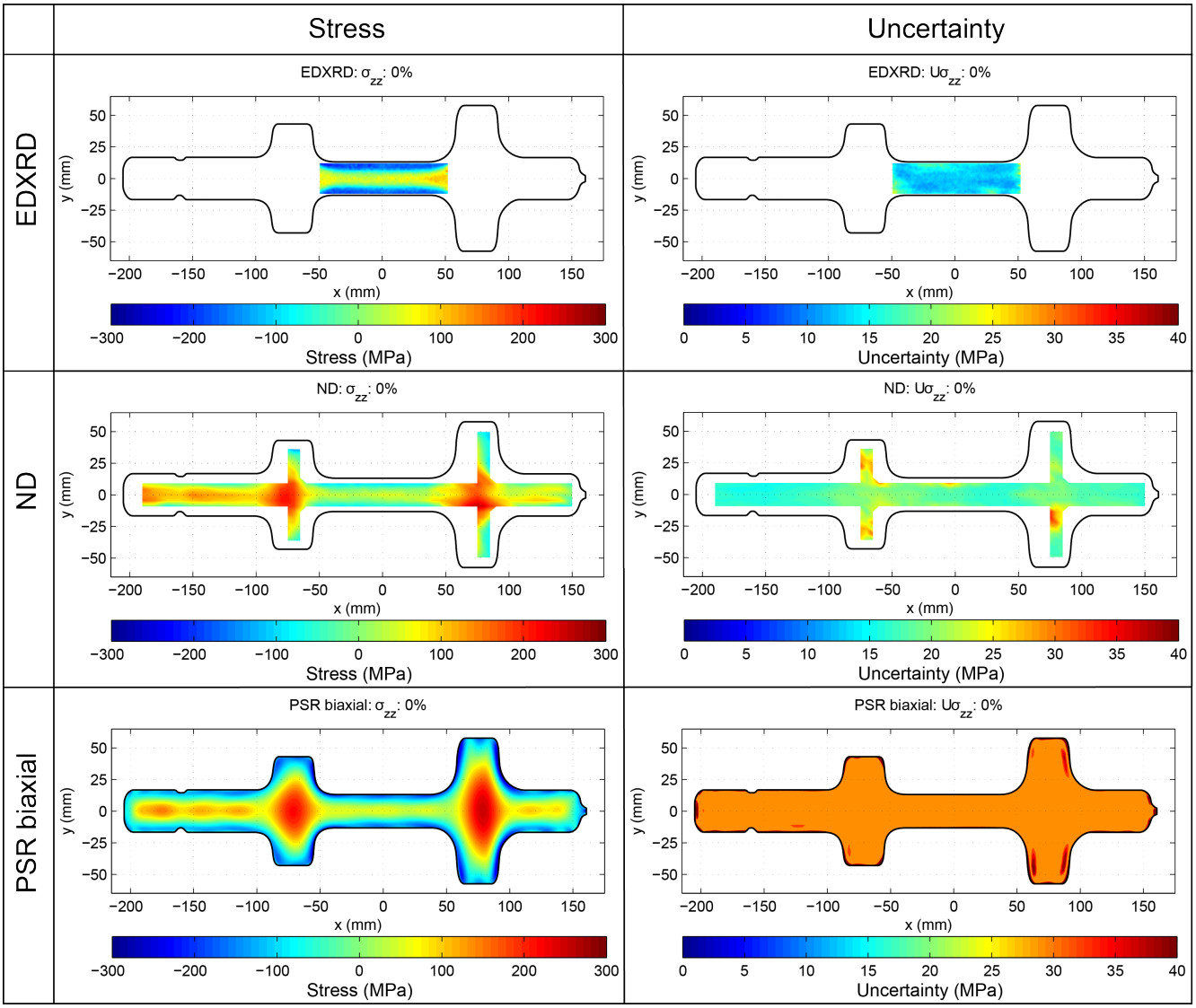

Figure 12: Measured stress and uncertainty (σ_{zz}) for the 0% cold-working condition. Top row is energy disspersive x-ray diffraction (EDXRD), second row is neutron diffraction (ND), and the third row is the Primary slice removal biaxial mapping (PSR). The left column is the stress and the right column is the uncertainty.

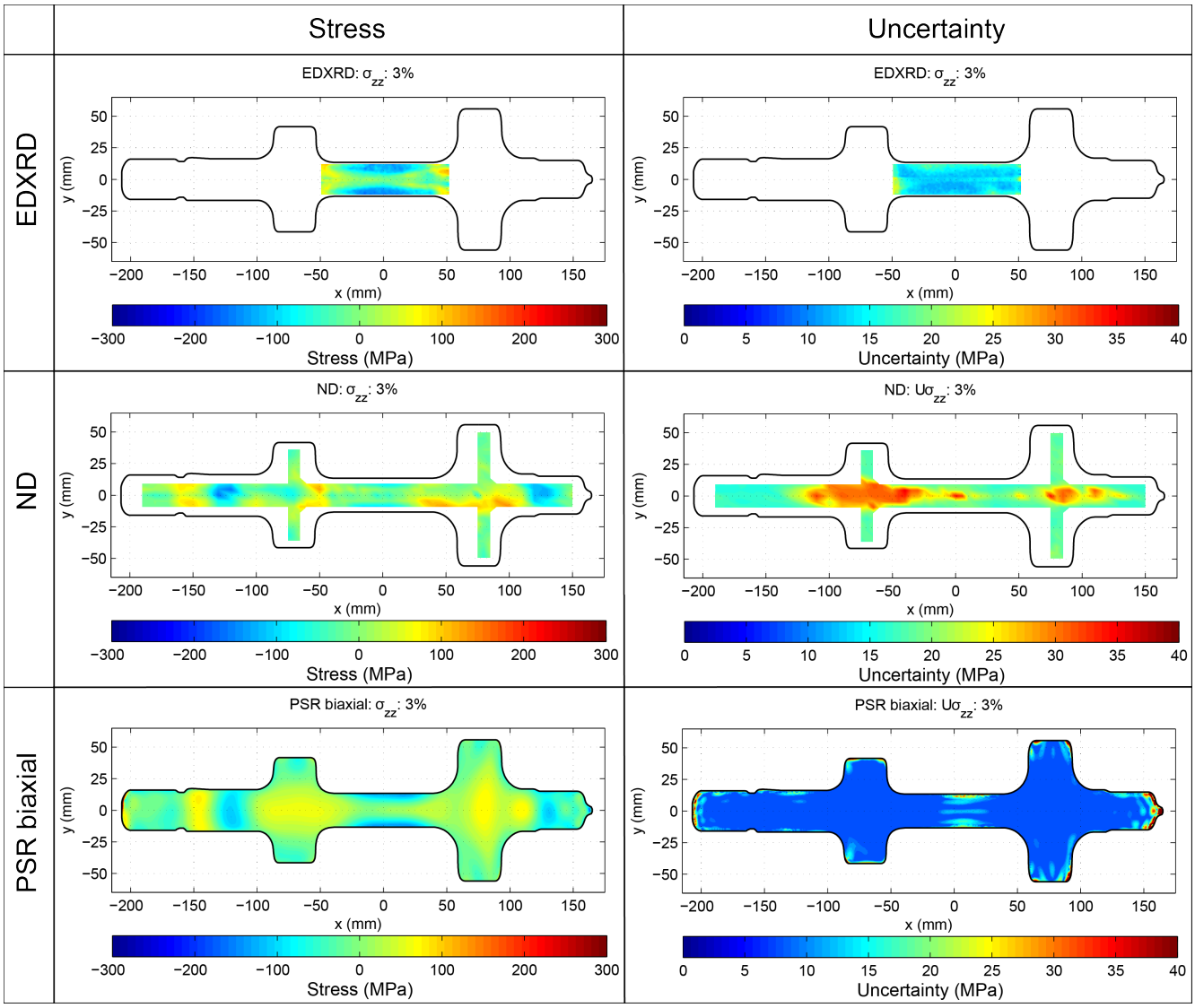

Figure 13: Measured stress and uncertainty (σ_{zz}) for the 3% cold-working condition. Top row is energy disspersive x-ray diffraction (EDXRD), second row is neutron diffraction (ND), and the third row is the Primary slice removal biaxial mapping (PSR). The left column is the stress and the right column is the uncertainty.

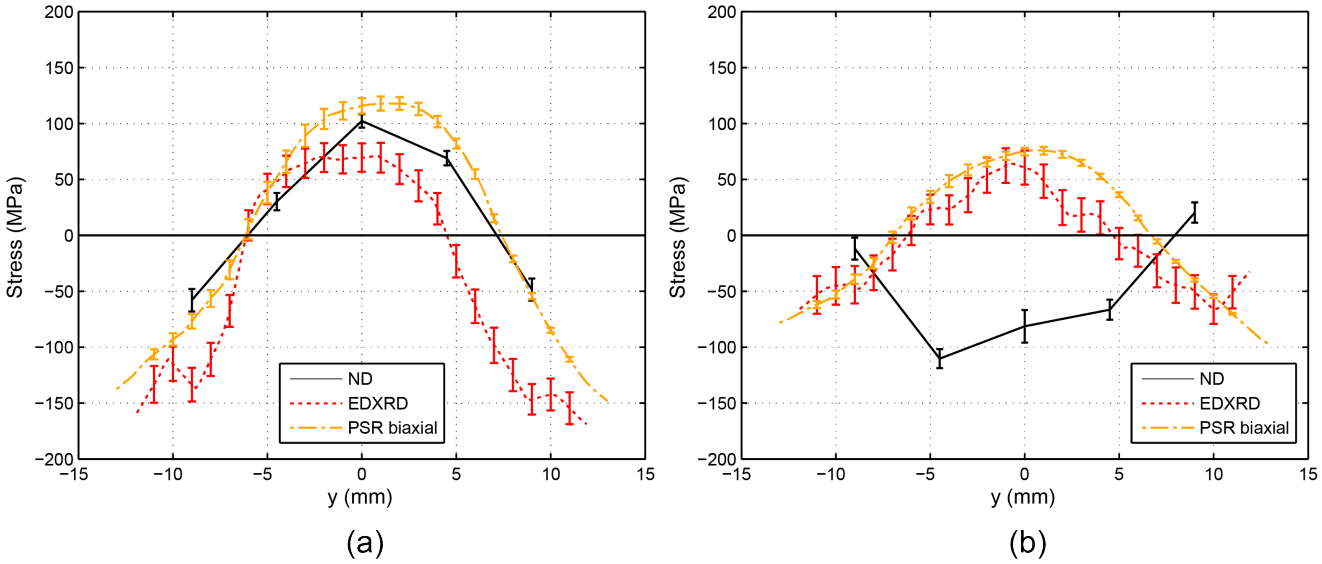

Figure 14: Line plots of the σ_{xx} stress from each of the measurement techniques along the line at x = 0 for the (a) 0% and (b) 3% cold-working conditions.

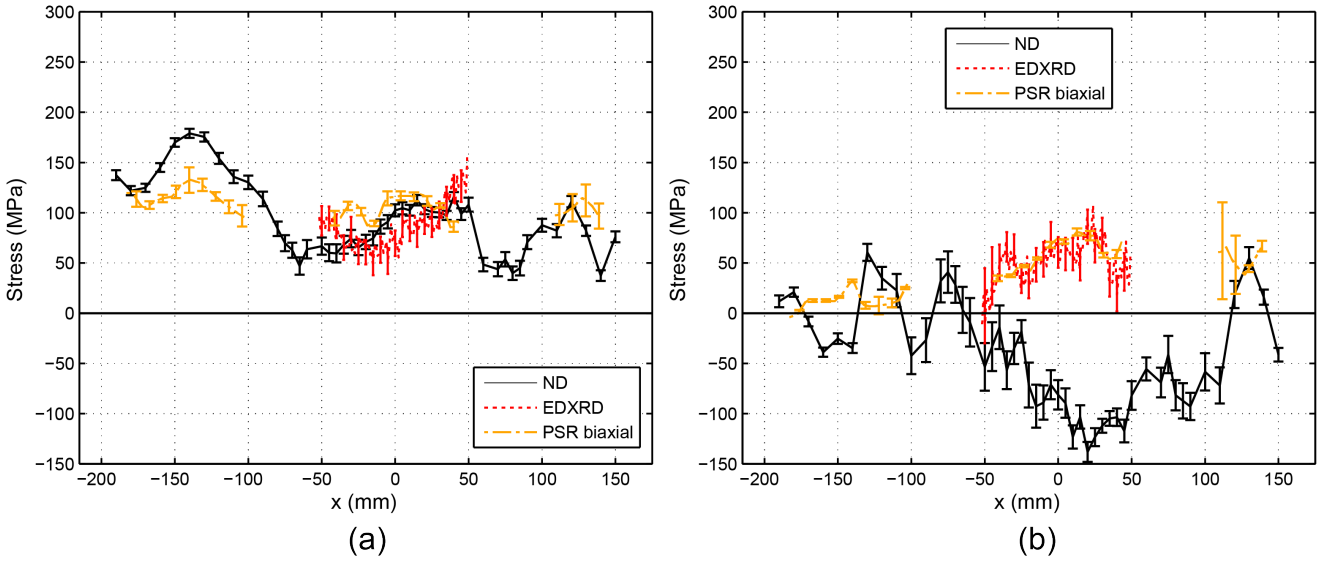

Figure 15: Line plots of the σ_{xx} stress from each of the measurements techniques along the line at y = 0 for the (a) 0% and (b) 3% cold-working conditions.

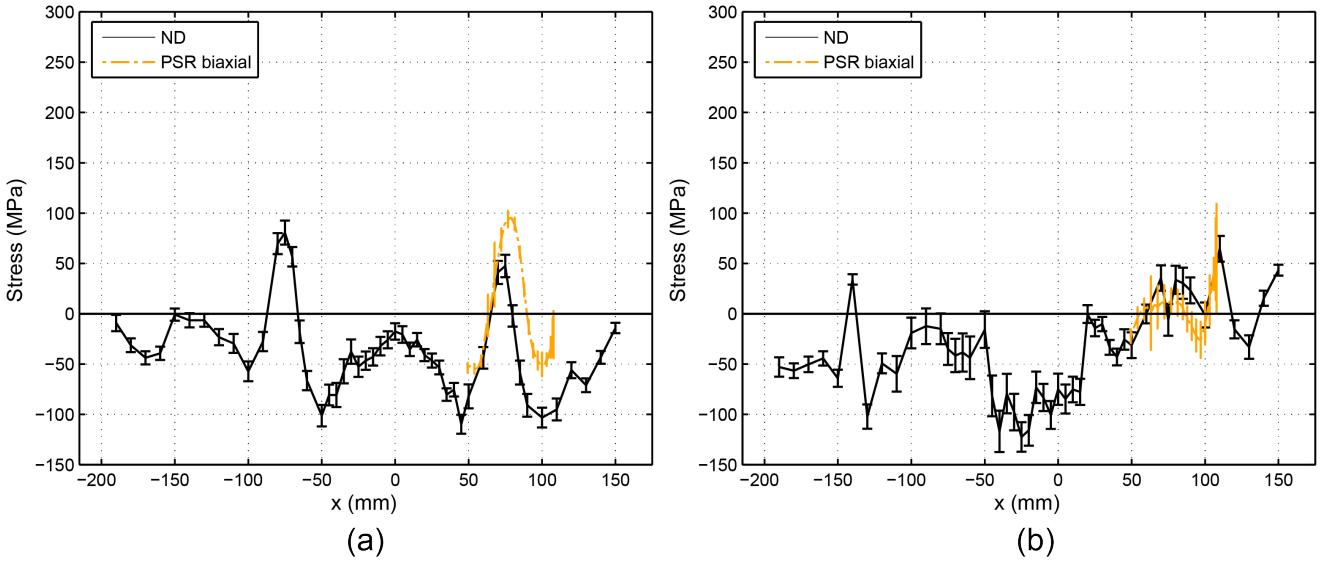

Figure 16: Line plots of the σ_{yy} stress from each of the measurements techniques along the line at y = 0 for the (a) 0% and (b) 3% cold-working conditions.

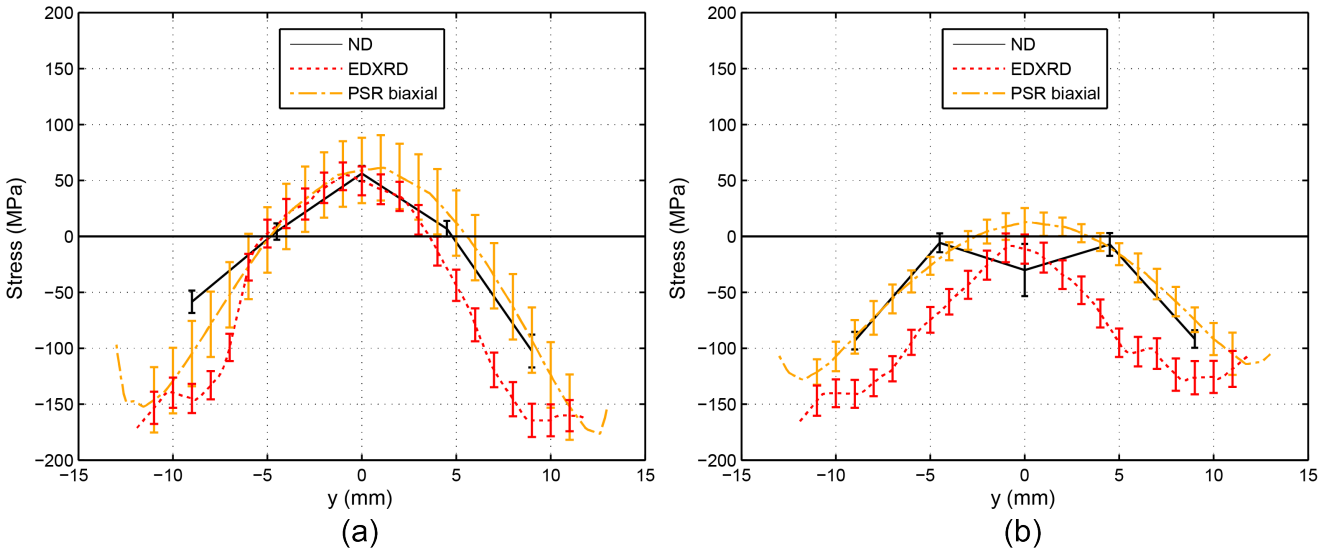

Figure 17: Line plots of the σ_{zz} stress from each of the measurements techniques along the line at x = 0 for the (a) 0% and (b) 3% cold-working conditions.

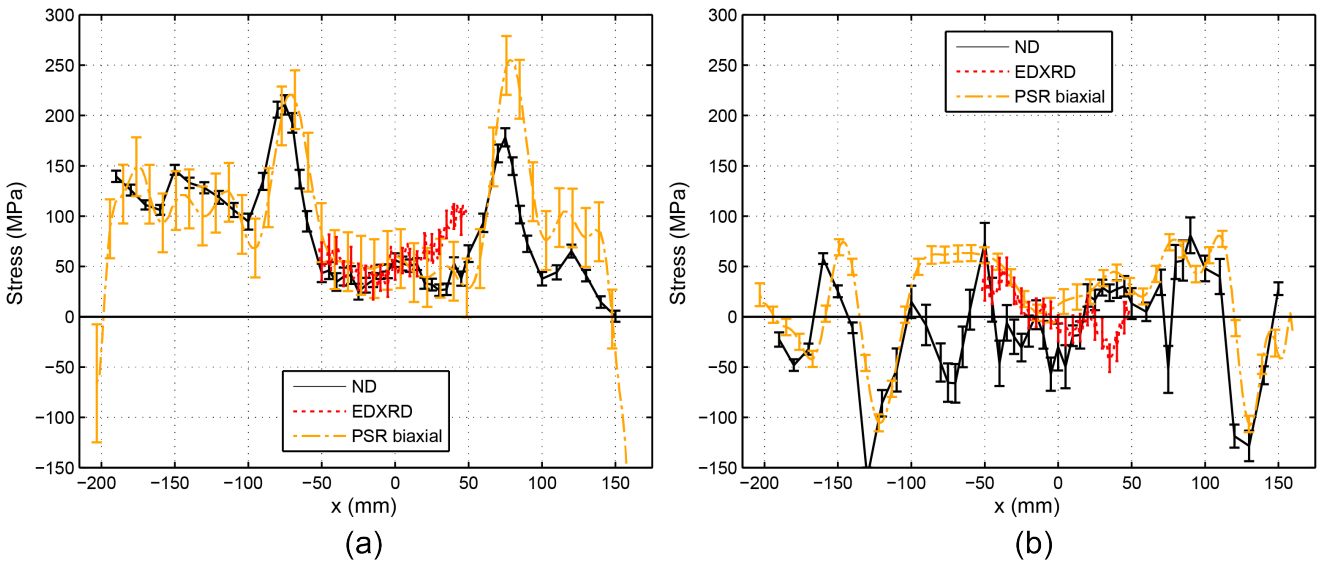

Figure 18: Line plots of the σ_{zz} stress from each of the measurements techniques along the line at y = 0 for the (a) 0% and (b) 3% cold-working conditions.

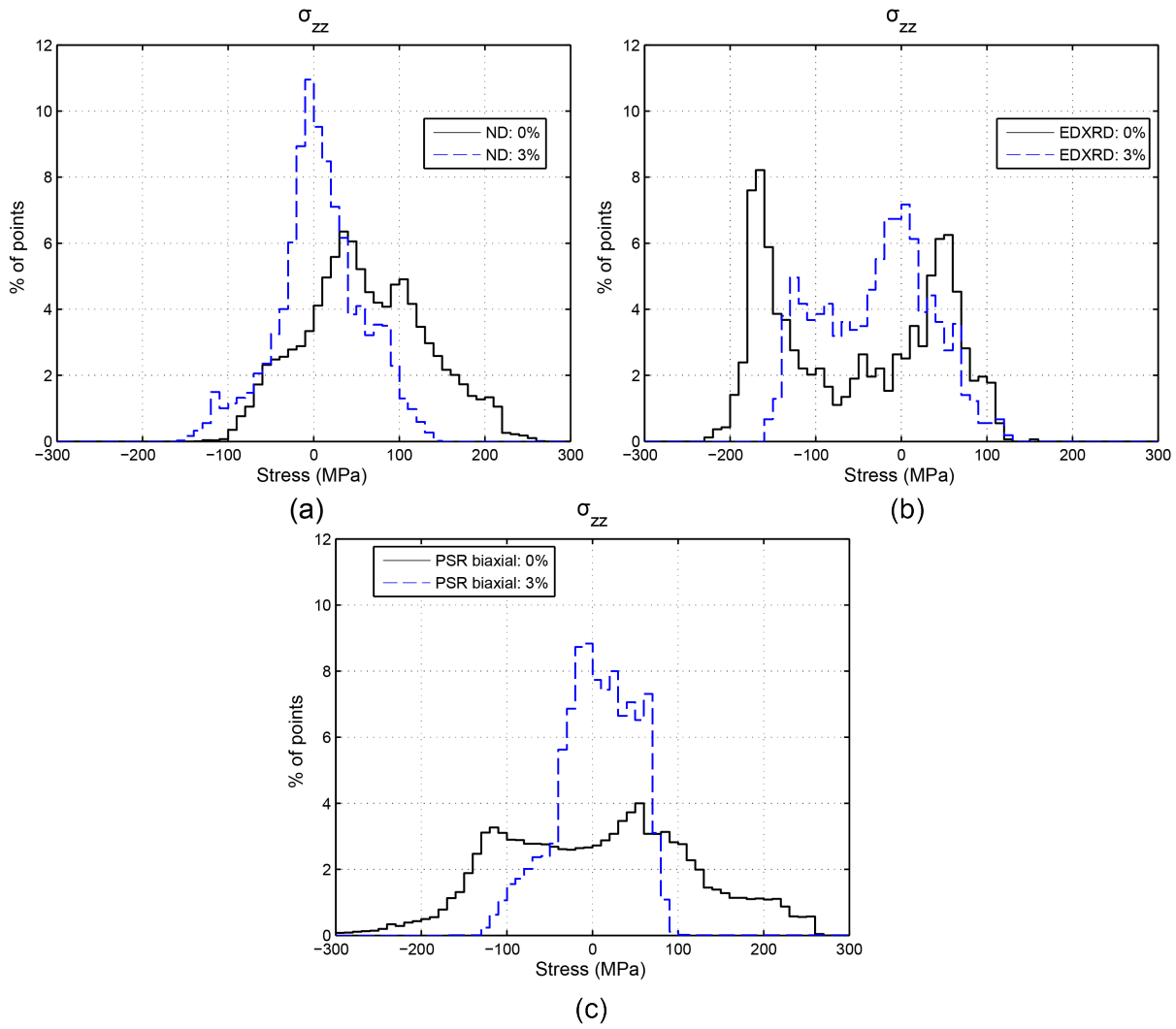

Figure 19: Histograms of all measurement techniques for the 0% and 3% cold worked conditions for (a) σ_{xx}, (b) σ_{yy}, and (c) σ_{zz}.

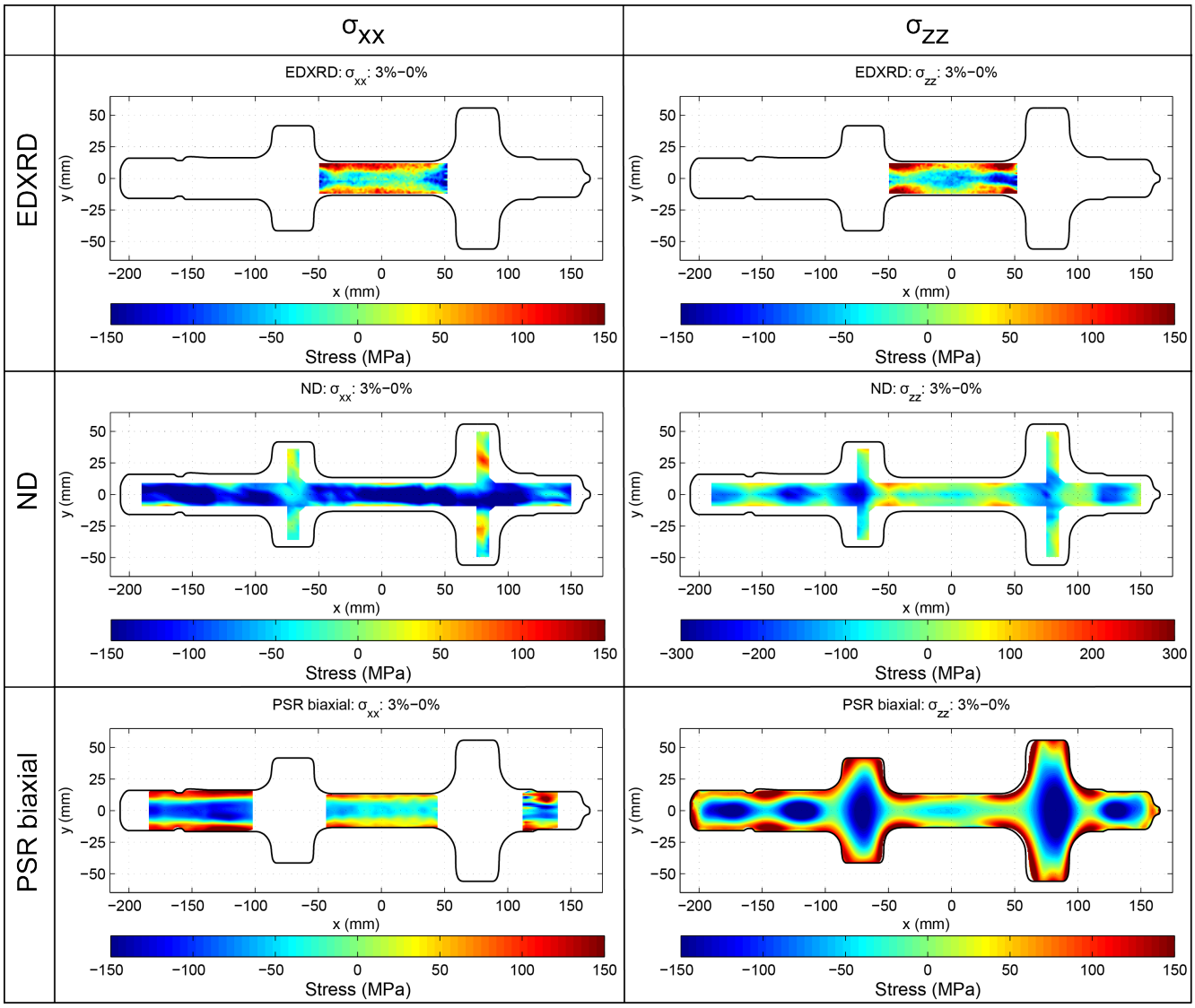

Figure 20: Stress difference (3% - 0% cold-working condition) for all three stress components and measurement techniques. Top row is energy disspersive x-ray diffraction (EDXRD), second row is neutron diffraction (ND), and the third row is the Primary slice removal biaxial mapping (PSR). The left column is σ_{xx} and the right column is σ_{zz}.

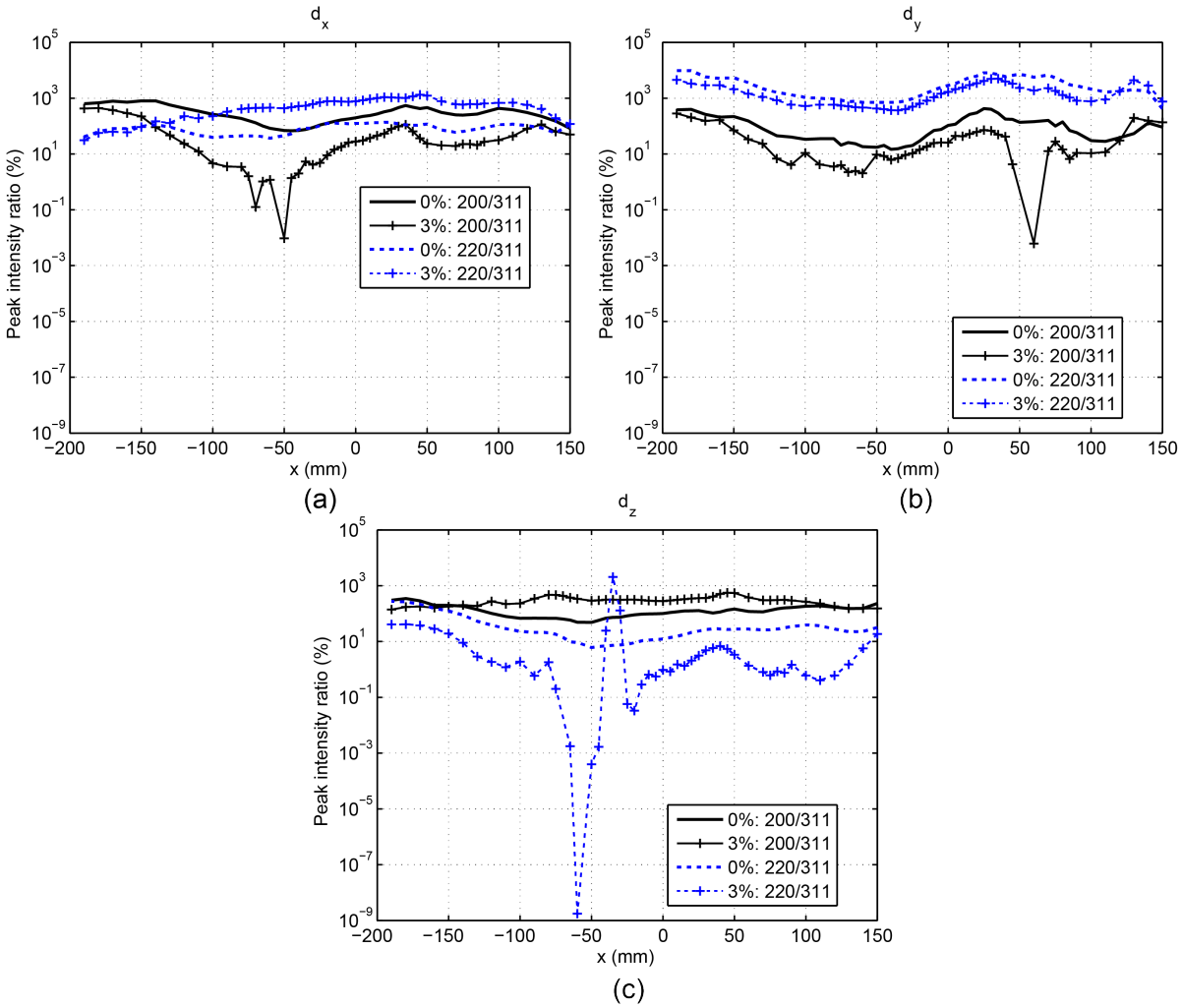

Figure 21: Ratio of the peak diffraction intensity of the {200} and {220} peaks relative to the {311} peak for the 0% and 3% forging specimens at y = 0 for (a) d_x, (b) d_y, and (c) d_z.